Type-II InAs/GaSb/AlSb superlattice-based heterojunction phototransistors: back to the future

Abbas Haddadi, Arash Dehzangi, Romain Chevallier, Thomas Yang and Manijeh Razeghi[1]

Center for Quantum Devices, Electrical Engineering and Computer Science Department,
Northwestern University, 2220 Campus Drive, Evanston, IL, USA 60208-0893

ABSTRACT

Most of reported HPTs in literatures are based on InGaAs compounds that cover NIR spectral region. However, InGaAs compounds provide limited cut-off wavelength tunability. In contrast, type-II superlattices (T2SLs) are a developing new material system with intrinsic advantages such as great flexibility in bandgap engineering, low growth and manufacturing cost, high-uniformity, auger recombination suppression, and high carrier effective mass that are becoming an attractive candidate for infrared detection and imaging from short-wavelength infrared to very long wavelength infrared regime. We present the recent advancements in T2SL-based heterojunction phototransistors in e–SWIR, MWIR and LWIR spectral ranges. A mid-wavelength infrared heterojunction phototransistor based on type-II InAs/AlSb/GaSb superlattices on GaSb substrate has been demonstrated. Then, we present the effect of vertical scaling on the optical and electrical performance of heterojunction phototransistors, where the performance of devices with different base width was compared as the base was scaled from 60 down to 40 nm.

1. INTRODUCTION

Rapidly growing use of the Internet and multimedia services has created congestion in the telecommunications networks and placed many new requirements on carriers. Customers want ultra-high-speed, multi-gigabit-per-second (multi-Gb/s) bandwidth, which is traditionally accomplished using optical fibers. However, installing new fiber optic cable to all customers is prohibitively expensive, especially in metropolitan areas. Free-space optical (FSO) communication is considered to be one of the key technologies for supplying high-bandwidth, “last-mile” connections to costumers without the need for optical fiber.[1] Using lasers as signal carriers, FSO laser communications can provide a line-of-sight, wireless, high-bandwidth, communication link between remote sites. FSO Laser-Com offers substantial advantages over conventional RF wireless communications technology, including higher data rates, low probability of intercept, low power requirements, and smaller packaging.[2, 3]

Near-infrared (NIR, $0.8 < \lambda < 2$ μm) FSO communication is also hampered by atmospheric scattering and absorption. Moving from the NIR towards the mid-wavelength infrared (MWIR, $3 < \lambda < 5$ μm) allows superior transmission through common atmospheric problems such as fog, clouds, and smoke. When coupled with improvements in MWIR laser and modulator design,[3-5] this makes possible reliable optical replacements for radio, microwave, and even NIR FSO communications links in many applications. This is driving a new demand for fast and sensitive MWIR photodetectors suitable for FSO communication. However, photodetector performance in the MWIR region is still behind the requirements of FSO communications. Achieving suitable performance will require developing a novel solution that can overcome current device limitations.

To date, most NIR optical receiver designs have employed pin photodiodes as photodetectors. However, these devices exhibit no internal/intrinsic gain, and increased capacitance due to their relatively large-area intrinsic absorption layer is known to be the limiting factor for high frequency operation of the photoreceiver. Metal-semiconductor-metal photodetectors, on the other hand, have low capacitance due to their Schottky contacts which make them suitable for high frequency operation but their temperature instability, lack of internal gain and complicated epitaxial growth and fabrication processes limit their use for MWIR optical receivers.

---

[1] razeghi@eecs.northwestern.edu; phone: (847) 491-7251; fax: (847) 467-1817; www.cqd.eecs.northwestern.edu

Quantum Sensing and Nano Electronics and Photonics XV, edited by Manijeh Razeghi, Gail J. Brown,
Jay S. Lewis, Giuseppe Leo, Proc. of SPIE Vol. 10540, 1054004 · © 2018 SPIE
CCC code: 0277-786X/18/$18 · doi: 10.1117/12.2297475

Heterojunction bipolar transistor (HBT) and heterojunction phototransistor (HPT) technology has seen recent rapid progress and is now one of the main options in several applications in wireless communication, power amplifier, or frequency synthesizer applications [6]. HPTs are an alternative technology that can demonstrate both high speed and internal gain.[5, 7, 8] Functionally, a HPT is a pin photodiode integrated with a bipolar transistor to form an integrated amplifier.[8] Unlike avalanche photodiodes [9], HPTs can provide large photocurrent gain without requiring high bias voltages or the excess avalanche noise characteristic of avalanche photodiode operation.[10]

HPT devices have demonstrated higher emitter injection efficiency compare to conventional homojunction phototransistors, with ability to create high internal gain [11]. Unlike homojunction phototransistors, HPTs have no requirement to have a heavily doped emitter with lightly doped base contact to give better emitter injection efficiency[12]. In fact, regardless of the comparative emitter-base doping concentration, HPTs can reach injection efficiencies close to unity because the reverse injection from base is blocked by the hetero-barrier. This means that in order to reduce the base-emitter capacitance and base resistance, as parasitic parameters, one can use a lightly doped emitter and heavily doped base in HPTs. [1]

Considered a promising infrared photodetector, HPTs low noise and large optical conversion gain at low bias voltages. [13] Early HPTs used InGaAs, and AlGaAs structure, which provided enhanced performance but, they were plagued with reliability and processing problems.[12, 14, 15] This led to new compound semiconductor technologies (e.g., InGaP, InP, SiGe) being proposed for HBT/HPT devices to minimize reliability and processing concerns. [14, 16-19]

Type-II superlattices (T2SL) material system and design can be a promising alternative for MWIR optical receivers. [20-22]

T2SLs are a developing material system [23-25] that has led to the development of high performance mid-wavelength infrared (MWIR) HPT [26]. This material system benefits from the advantages of high flexibility in bandgap engineering [21], high carrier effective mass [27, 28], good uniformity [29], good imaging performance and auger recombination suppression[30, 31]. T2SLs have become a remarkable candidate for IR detection and imaging [32-34] covering the full span from short-wavelength infrared (SWIR) toward very-long wavelength infrared (VLWIR)[35]. The T2SL based HPTs can also be a possible solution to the urgent demand for sensitive MWIR photodetectors for MWIR free-space optical (FSO) communication as well as high-speed sensitive MWIR imagers.[26]

In this paper, first we report the demonstration of a MWIR HPT based on T2SL with 60 nm base thickness. Such devices can be used for making both MWIR FSO systems and high-speed sensitive MWIR imagers. Then we present the impact of scaling of the base thickness (w_B), down to 40 nm, on optical and electrical performance of MWIR HPT devices.

2. HETEROJUNCTION PHOTOTRANSISTORS BASED ON TYPE-II SUPERLATTICES

An npn HPT structure was chosen to be used in this study. The device consists of a n-doped M-structure-based[27] wide-bandgap emitter, a p-doped T2SL-based base, and a lightly doped n-type T2SL-based collector.[26] The emitter superlattice design consists of 7/1/5/1 mono-layers (MLs) of InAs/GaSb/AlSb/GaSb, respectively, per period with a ~650 meV bandgap at 77 K. For the base and collector regions a design of 6.5 MLs of InAs and 12 MLs of GaSb per period[36] were used with one binary InSb interface and the other interface being InGaSb to reduce the mismatch. The schematic of the device structure is illustrated in Figure 1.

The incident MWIR light is absorbed in the T2SL-based base and collector regions, creating electron-hole pairs. In this device, the collector region is completely depleted; therefore, drift is the main transport mechanism inside the collector region that helps faster transfer of photo-generated holes from the collector region to the base region. The photo-generated holes accumulate in the base and alter the base-emitter potential so that electrons are injected from the emitter into the base, and enter the collector region.[8] Current gain in this device is achieved by normal transistor action when w_B is less than the diffusion length (L_n) of the injected electrons.[37]

The material for this study was grown using a GEN II molecular beam epitaxy (MBE) reactor, equipped with group-III SUMO® cells and group-V valved crackers, on a Tellurium-doped (10^{18} cm^{-3}) n^+-GaSb substrate. The growth was started with a 100 nm GaSb layer followed by a 0.5 μm *n*-doped $InAs_{0.91}Sb_{0.09}$ buffer layer (10^{18} cm^{-3}). The device structure was started by growing an *n*-type (10^{18} cm^{-3}) 0.5 μm-thick contact layer. The contact layer superlattice design is the same as the emitter region. Then, the 0.5 μm-thick wide-bandgap *n*-doped (~10^{17} cm^{-3}) emitter was grown. This was followed by growing a 60 nm-thick *p*-doped base layer (~6×10^{16} cm^{-3}), a 1 μm-thick *n*-doped collector/absorption region (~5×10^{15} cm^{-3}), and a 500 nm *p*-type top contact (10^{18} cm^{-3}). The base, collector and top contact regions share the same superlattice design. Silicon (Si) and beryllium (Be) were used as the *n*- and *p*-type dopants, respectively.

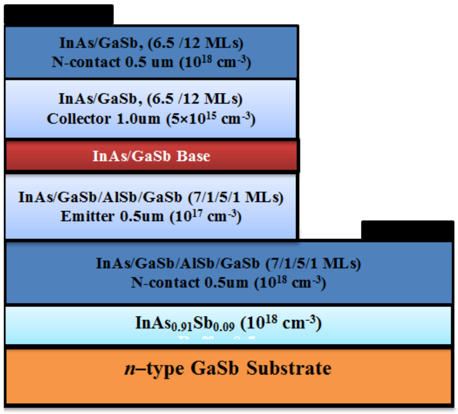

Figure 1. Schematic of the MWIR HPT design and structure. The incident light is absorbed in the T2SL-based base and collector regions, creating electron-hole pairs.

The grown sample was processed into a set of unpassivated mesa-isolated test structures with device sizes ranging from 100×100 to 400×400 μm^2 using standard photo-lithographic processing techniques which were used for T2SL-based photodetectors.[38] The phototransistors were left unpassivated but carefully treated, by performing many surface cleaning steps, in order to minimize the surface leakage. Then, the sample was wire-bonded to a 68 pin leadless ceramic chip carrier (LCCC). The emitter and collector terminals of each device were wire-bonded while the base terminal was left floating. For simplicity, in the rest of this paper, we will refer to the collector–emitter bias voltage, V_{CE}, as the applied bias voltage. Finally, the sample was loaded into a cryostat for both electrical and optical characterization at 77 and 150 K.

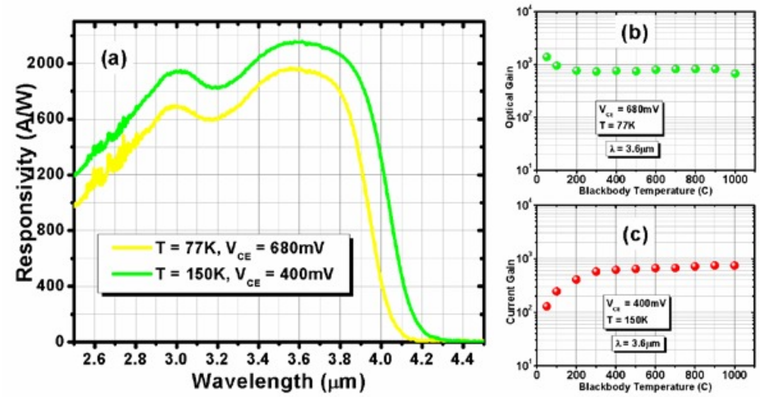

Figure 2. (a) Saturated responsivity spectrum of the device at 77K under 680mV applied bias (V_{CE}) and at 150K under 400mV applied bias in front-side illumination configuration without any anti-reflection coating. The device optical gain around 3.6μm vs blackbody temperature/optical power density (b) at 77K and (c) 150K.

The optical characterization was done in front-side illumination configuration without applying any anti-reflection (AR) coating to the phototransistors. A Bruker IFS 66v/S Fourier transform infrared spectrometer (FTIR) was used to measure the spectral response of the phototransistor. The absolute responsivity (R_i) of the phototransistor was measured with a calibrated blackbody source at 1000 °C. The optical performance of the devices is shown in Figure 2. The device exhibits a 50% cut-off wavelength of ~3.95 μm at 77 K as predicted from the band structure calculations. The device responsivity reaches a peak value of 1960 A/W around 3.6 μm under 680 mV applied bias for a 1 μm-thick collector/absorption region at 77 K. At 150 K, the device shows a 50% cut-off wavelength of ~4.05 μm. The device responsivity reaches a peak of 2152 A/W around 3.6 μm under 400 mV applied bias. The peak responsivity starts to saturate under bias voltages higher than 600 and 300 mV at 77 and 150 K, respectively. At higher bias voltages, the combination of the dark current and photocurrent becomes higher than the input current limit of our transimpedance amplifier; thus, we performed optical characterization up to 680 and 400 mV applied bias voltages at 77 and 150 K, respectively.

In order to study the effect of incoming optical power on the device's optical gain (*G_{opt}*), we swept the blackbody temperature from 1000 °C down to 50 °C and measured the optical gain at different blackbody temperatures for different saturation applied biases at 77 and 150 K operating temperatures. In a HPT device, *G_{opt}* is proportional to the current gain of the device as [39]:

$$G_{opt} \propto (1+\beta) \propto \left(1+\left[\cosh\left({}^{W_B}/_{L_n}\right)-1\right]^{-1}\right) \qquad (1)$$

where the second term is extracted from the Equation 1. The optical gain of the phototransistor is the ratio of the number of photo-generated carriers creating the photocurrent to the number of incident photons. In order to study the variation of optical gain versus applied bias, the same calibrated blackbody source at 1000 °C was used. At 77 K, the device optical gain becomes unity under 200 mV applied bias. The optical gain increases with increasing applied bias and reaches its saturation value of 668 at bias voltages higher than ~600 mV. In contrast, the device optical gain becomes unity at 150 K under 110 mV applied bias. The optical gain at this operating temperature saturates at bias voltages higher than 350mV. The saturated optical gain at 150K is 639.

In order to study the effect of incoming optical power on the device optical gain, we swept the blackbody temperature from 1000 °C down to 50 °C and measured the optical gain under 680 and 400 mV applied biases at 77 and 150 K operating temperatures, respectively. Figure 2 (b) and (c) present the optical gain of the device versus the blackbody temperature. The device shows very small gain change over a broad range of optical power in which reveals a high dynamic range.

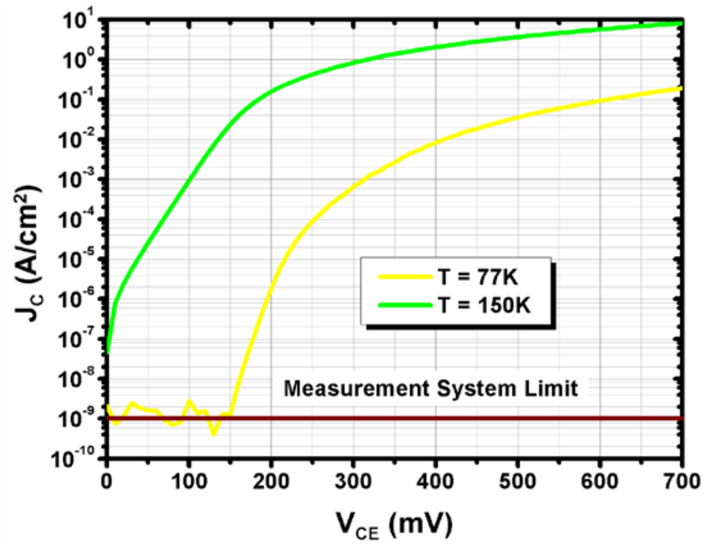

Figure 3. Collector dark current density vs. applied bias voltage characteristic of the device at 77K and 150K.

Figure 3 presents the collector dark current density (J_C) versus applied bias voltage. At 77 K, the sample exhibits a unity optical gain collector dark current density of 1.8×10^{-6} A/cm^2 under 200 mV applied bias, whereas at 150 K, the unity optical gain collector dark current density at 110 mV is 1×10^{-3} A/cm^2. The variation of the inverse of the R×A (at 600 mV) with the perimeter over area ratio (not shown here) proved that surface leakage is the main source of the dark current in our devices. In order to calculate the DC current gain (β) of the phototransistor, a photodiode with the same absorption region design and thickness (1 μm) was grown and optically characterized. Its responsivity value was 0.5 and 0.58 A/W around 3.6 μm at 77 and 150 K, respectively; this provides an estimate of the generated photocurrent inside the collector region. One can calculate the DC current gain by dividing the phototransistor responsivity into the photodiode responsivity at the same wavelength (in this case around 3.6 μm). The device exhibits a saturated DC current gain of 3881 and 3710 at 77 and 150 K, respectively. We will explain the gain calculation later in next section.

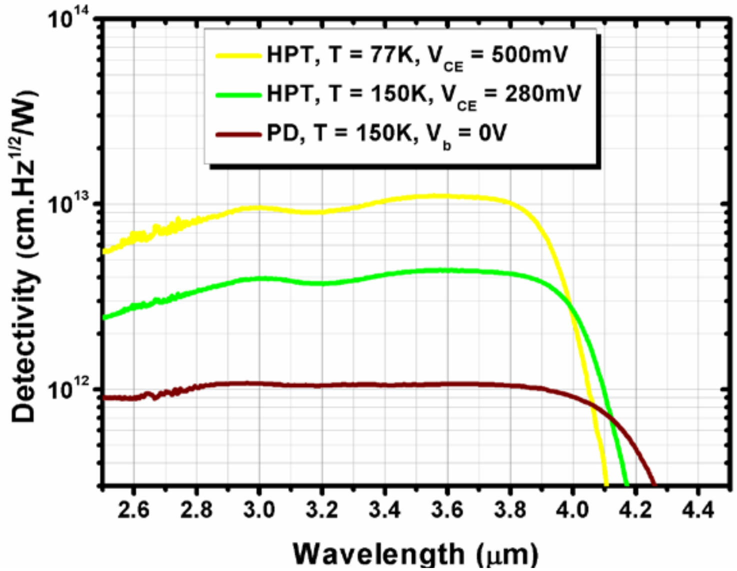

Figure 4. (a) Specific detectivity (D^*) spectrum comparison between HPT operating at 77 and 150K with a T2SL-based MWIR heterojunction photodiode (PD) operating at 150K in front-side illumination configuration without any anti-reflection coating.

After performing optical and electrical characterization, the specific detectivity was calculated. The shot noise limited detectivity (D*) is defined as:

$$D^* = R_i\left[2qJ_c + {}^{4k_BT}\!/_{R_A}\right]^{-1/2} \qquad (2)$$

where T is the temperature, k_B is the Boltzmann constant, J_C is the dark current density, and R_A is the differential resistance area product. The specific detectivity (D^*) was calculated for the phototransistor at 77 and 150 K. The device exhibits a saturated dark current shot noise limited specific detectivity of 1.1×10^{13} cm·Hz$^{1/2}$/W under 500 mV of applied bias at 77 K (Figure 4) for a fully immersed 300 K background with a 2p field-of-view (FOV). At 150 K, the device exhibits a specific detectivity of 4.4×10^{12} cm·Hz$^{1/2}$/W under 280 mV applied bias (Figure 4) for the same background condition. Figure 4 also shows a comparison between the specific detectivity values of the phototransistor at 77 and 150 K with a state-of-the-art T2SL-based heterojunction photodiode[40] operating at 150 K. The phototransistor exhibits a specific detectivity value that is four times higher than the photodiode at 150K. Moreover, the phototransistor generates more photo-current than the photodiode for the same incoming optical power (2–3 orders of magnitude) which can be used for making imagers hundreds of times faster and more sensitive than current photodiode-based imagers.

In addition, the specific detectivity spectrum stays almost constant over a broad range of wavelengths (Figure 4) which makes this phototransistor a promising choice for MWIR infrared imaging applications.

3. STUDY OF VERTICAL SCALING ON PERFORMANCE OF HETEROJUNCTION PHOTOTRANSISTOR

Scaling the size of semiconductor devices provides a remarkable enhancement in performance. During the last decades, the principle of shrinking the semiconductor device dimensions has created an extraordinary success in semiconductor industry. This includes all types of transistors, including the metal oxide field effect transistors (MOSFETs) and bipolar transistors[41-43]. Recently, bipolar technology evolution managed to overcome the limitations in the course of scaling, using novel material system and structural innovations.[44] In this matter vertical scaling has appeared to be a major driving force for the evolution of bipolar transistors. In the case of vertical scaling, collector and base scaling have the main effect on performance of the bipolar transistors.[45, 46] In this work, we present the impact of scaling the base on optical and electrical performance of MWIR HPT devices. The w_B of the device is scaled down to 40 nm, and we compare the optical and electrical parameters of the devices with different w_B at 77 K and 150 K. The general details of the growth, design, structure and fabrication of the HPT device were explained earlier in this paper.

As explained earlier, the T2SL HPT structure has two-terminals with a floating base contact. The charge transition mechanism is based on the creation of electron-hole pairs in the base and collector regions due to the absorbance of incident MWIR light. This leads to accumulation of photo-generated holes in the base, which changes the potential level of the base region and increases the forward bias of the emitter-base junction.

Electrons, on the other hand, are injected from the emitter into the base, and cross the base toward the collector region[8]. When the emitter-base junction is forward biased, a wide-bandgap emitter can provide emitter-base injection efficiency close to unity, since the valence-band barrier effectively eliminates hole injection from base to emitter [8]. The DC current gain of the phototransistor (β) can be written as following [39]:

$$\beta \approx \left[cosh\left({}^{w_B}/_{L_n}\right) - 1\right]^{-1} \qquad (3)$$

Where w_B is the base thickness and L_n is the minority carrier diffusion length in the base region. According to Equation 3, β is limited by the base transport factor [39]. High current gain in HPT devices is strongly related to w_B, especially when it is smaller than the L_n in the base region. In fact, w_B has a remarkable role in the device performance, and by changing w_B we can monitor and optimize the current gain and thus the device performance. The main purpose of this study is to investigate the impact of w_B scaling on the optical and electrical performance of HPT device.

The optical performance (saturated responsivity spectrum) of the devices is shown in Figure 5, at 77 K under V_{CE} of 680 mV, 500 mV and 230 mV (a), and under V_{CE} of 400 mV, 300 mV and 140 mV at 150 K (b). The devices exhibit 50% cut-off wavelength at ~3.95 μm, ~3.91 μm and ~3.93 μm at 77 K for the devices with 60 nm, 50 nm and 40 nm base thickness, respectively. The 50% cut-off wavelength at 150 K for the devices with 60 nm, 50 nm and 40 nm base thicknesses are ~4.09 μm, ~4.05 μm and ~4.10 μm, respectively. The responsivity of a phototransistor (R_i) is defined as a ratio of photogenerated current to incident optical power as [47]:

$$R_i = {}^{\beta I_{ph}}/_{P_{in}} \qquad (4)$$

where I_{ph} is the photogenerated current and P_{in} is incident optical power. Merging Equation 3 and 4 reveals the reverse proportionality of the responsivity of HPT device with w_B, as following:

$$R_i \approx {}^{I_{ph}}/_{P_{in}\left[cosh\left({}^{w_B}/_{L_n}\right) - 1\right]} \qquad (5)$$

Figure 5 (c,d) shows the responsivity measurement results at 3.6 μm as a function of applied bias voltage, V_{CE}, with different w_B at 77 and 150 K. As an overall trend, at both 77 K and 150 K the responsivity values first increase linearly with raising V_{CE} and then start to saturate. At 77K at wavelength of 3.6 µm, the saturated responsivity reaches 8845 A/W under V_{CE}=230mV, 4882 A/W under V_{CE}=500mV and 1940 A/W under V_{CE}=680mV for the device with 40nm, 50nm and 60nm base thickness, respectively (Figure 5c). As predicted by Equation (5), the responsivity values increase with downward scaling of w_B. The saturated responsivity for the device with $w_B = 40$ nm is almost five times greater than the device with w_B = 60 nm. The same trend was observed at 150 K (Figure 5d), where the responsivity peak values were 9528 A/W (V_{CE}=140 mV), 5875 A/W (V_{CE}=300 mV) and 2151 A/W (V_{CE}=400 mV) for the device with 40 nm, 50 nm and 60 nm base thickness.

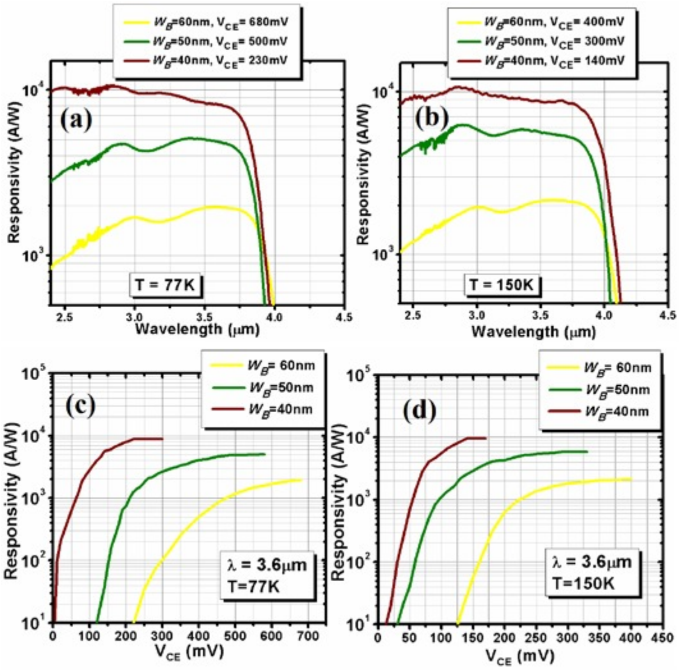

Figure 5. (a) Saturated responsivity spectrum of the devices (a) at 77 K under 680 mV, 500 mV and 230 mV applied bias (V_{CE}), (b) at 150 K under 400 mV 300 mV and 140 mV applied bias (V_{CE}) in front-side illumination configuration without any anti-reflection coating, for the devices with 60 nm, 50 nm and 40 nm base width, respectively. Responsivity measurements of the MWIR HPT devices around 3.6 µm vs. applied bias (V_{CE}) at 77K (c) and 150 K (d), with 60nm, 50nm and 40nm base widths.

As shown in Figure 5, there is a strong bias dependency of photo-responsivity for the HPT detector; the responsivity values increases by more than three orders of magnitude by increasing bias voltage from zero to saturation voltage for both 77 K and 150 K. When V_{CE} is increased, holes generated by photo-excitation are swept towards the base, which in turn reduces the potential barrier for electrons in the emitter-base junction. This facilitates injection of electrons from the emitter across the base toward the collector. Shrinking the base leads to more efficient emitter injection into the base at higher bias voltage and this results in amplification of the photocurrent due to the higher current gain[48]. The responsivity value increases at both operation temperatures, which is related to higher emitter-base injection efficiency as w_B is becomes smaller than L_n in the base region. In addition, it is possible that the thinner base can reduce recapture mechanism, which also can be another reason for better responsivity performance for the devices with thinner w_B [49]. Faster transport of injection for thinner w_B which leads to a higher gain can also explain why saturation for responsivity values takes place at smaller V_{CE}.

Figure 6 (a,b) present G_{opt} of the HPT devices around wavelength of 3.6 mm versus blackbody temperature for the w_B of 60 nm, 50 nm and 40 nm. The devices show small gain change over ~25 dB change of optical power.[19] As predicted from Equation (1), Figure 6 reveals that scaling of the base thickness results in increasing of G_{opt} for both 77 and 150 K, which is sign of better injection efficiency. For the blackbody source temperature of 1000 °C, the saturated G_{opt} values at 77 K were 668 for w_B = 60 nm, 1919 for w_B = 50 nm and 2760 for w_B = 40 nm under saturated V_{CE} bias (Figure 6a). At 150 K, the G_{opt} values were measured as 639 for w_B = 60 nm, 2168 for w_B = 50 nm and 3081 for w_B = 40 nm under saturated V_{CE} bias (Figure 6b). At both operating temperatures, the optical gain curve is relatively flat for a broad range of incident power levels (different blackbody temperatures), especially for the device with thinner w_B, which is indicative of the high sensitivity of the HPT device.

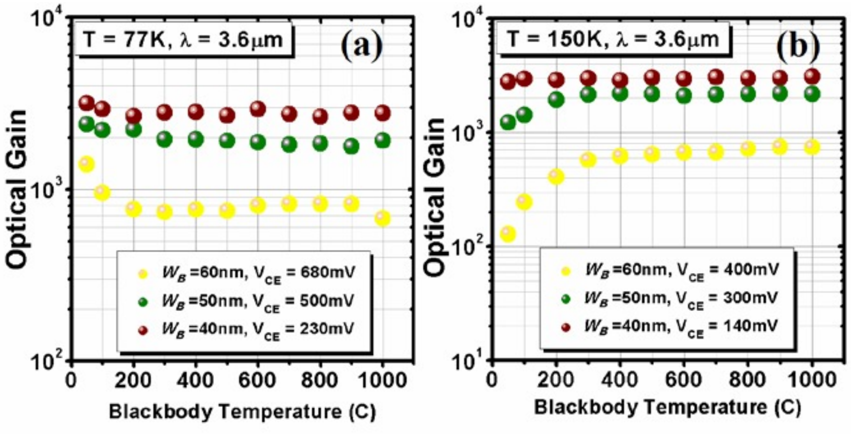

Figure 6. The device optical gain around 3.6 lm vs. blackbody temperature/optical power density at 77 K (a) and 150 K(b), under saturated V_{CE} bias for the devices with 60nm, 50nm and 40nm base widths

At 150 K, for the device with 60 nm base thickness at lower black body temperatures (<200 C°), the gain is found to have small power dependence, as a drop in G_{opt} value. This is probably related to higher recombination rate in the base for the device with wider w_B at higher temperature. Upon applying bias voltage and injection of electrons into the base region, recombination rate has important role to degrade optical gain of a HPT device. For a thinner w_B, as the electrons spend less time in the base on their way toward the collector, the recombination rate becomes minimized and more carriers are able to reach the collector. This is another way to explain the increased optical gain as base thickness is decreased.

The electrical performance of the devices has also been measured at different temperatures. Figure 7 (a,b) present J_C vs. applied bias voltage characteristics of the device, at 77 K and 150 K. At 77 K, the unity optical gain dark current density for the samples were measured as 1.8×10^{-6} A/cm^2 (V_{CE}= 200mV), 1.3×10^{-4}A/cm^2 (V_{CE}= 115mV) and 1.1×10^{-3} A/cm^2 (V_{CE}= 39 mV) for w_B of 60 nm, 50 nm and 40 nm, respectively.

At the higher temperature of 150K, the unity optical gain dark current density values increase to 4.5×10^{-4} A/cm^2 (V_{CE}= 110 mV), 1.2×10^{-3} A/cm^2 (V_{CE}= 40 mV) and 6.4×10^{-1} A/cm^2 (V_{CE}= 9 mV) for w_B of 60 nm, 50 nm and 40 nm, respectively. By scaling base thickness, there is an increasing trend of the dark current at both operation temperatures, and in order to address this trend, we need to calculate b values.

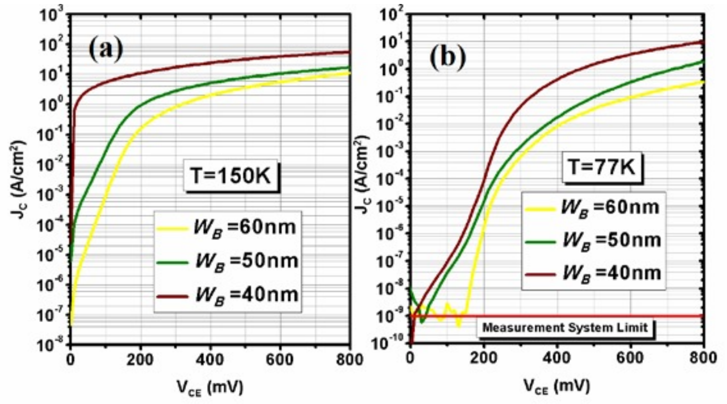

Figure 7. Collector dark current density vs. applied bias voltage characteristic at 77K (a) and 150K(b).

To calculate the b value of the phototransistor, optical characterization of a grown conventional photodiode with the same absorption region design and thickness was used [26]. This can provide an estimation of generated photocurrent inside the collector region. The responsivity value for this conventional photodiode at 3.6 μm was 0.50 A/W at 77 K and

0.58 A/W at 150 K. The current gain then is calculated by dividing the phototransistor responsivity over the photodiode responsivity at the same wavelength. The HPT device exhibits saturated *b* values of 3881, 9764 and 17690 at 77 K, as well as 3710, 11740 and 19050 at 150 K. Scaling down the base thickness results in a remarkable enhancement in the *b* value showing the excellent optical performance of the HPT devices. The increase of *b* with decreasing w_B, can be explained by the increasing J_C in Figure 7. By scaling w_B from 60 nm to 50 nm, the J_C value increases both for 77 K and 150 K. This trend is even more pronounced when w_B is reduced down to 40 nm, especially at 150 K, where J_C increases by almost one order of magnitude. This is probably related to involvement of different mechanisms, e.g. tunneling, in charge transmission, for the HPTs with a 40 nm base thickness.

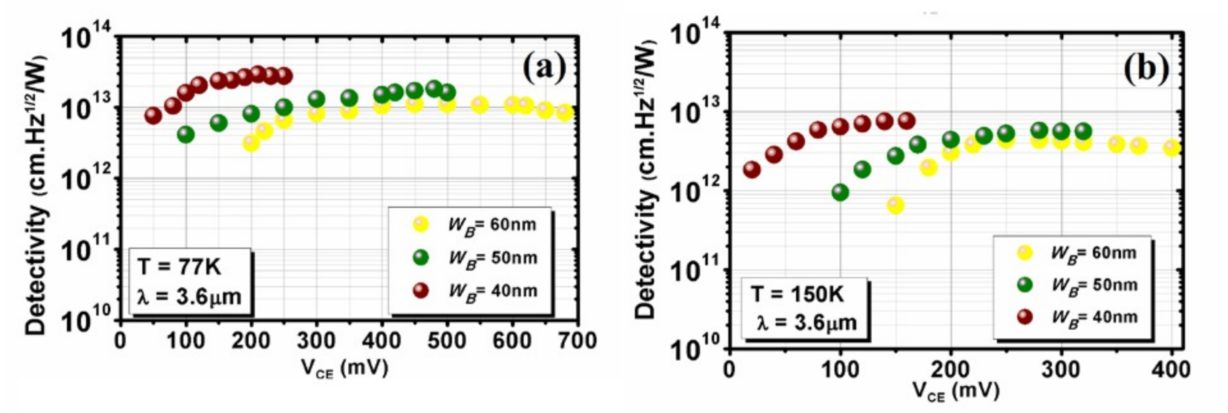

Figure 8. (a) Specific detectivity (D*)of the phototransistor around 3.6mm versus applied bias voltage at (a) 77K and (b) 150 K, with 60nm, 50nm and 40nm base widths

For a fully immersed 300 K background with 2p field-of-view (FOV) at 77 K and under saturated V_{CE} bias, the devices exhibited D* of 9.1×10^{12} cm·Hz$^{1/2}$/W for w_B = 60 nm, 1.6×10^{13} cm·Hz$^{1/2}$/W for w_B = 50 nm and 2.7×10^{13} cm·Hz$^{1/2}$/W for w_B = 40 nm. At 150K, the same trend was detected at saturated V_{CE} bias, where the devices exhibited the D* value of 3.4×10^{12} cm·Hz$^{1/2}$/W, 5.6×10^{12} cm·Hz$^{1/2}$/W and 7.5×10^{12} cm·Hz$^{1/2}$/W for w_B of 60 nm, 50 nm and 40 nm, respectively. Figure 8 demonstrates the phototransistor specific detectivity versus applied bias at wavelength around 3.6 mm for different w_B, at 77 (a) and 150K (b). By shrinking the base thickness D* increases at both operating temperatures; however, this trend is more pronounced for 77 K. As it can be seen, the D* values remain reasonably constant in a broad range of applied bias, at both temperatures. The small change in D* at lower V_{CE} values is recognizable for the device with w_B = 60 nm. As explained before, this trend is related to the higher rate of recombination in this specific device; since carriers spend more time in the base for devices with thicker base, there is more chance for them to be recombined compared to in device with thinner base. For the device with thinner base (w_B = 40 nm) the drop in D* values is less pronounced at both operational temperatures (Figure 8b), which is in agreement with the abovementioned discussion.

4. CONCLUSION

In this paper, the latest result abut T2SL base HPT device is demonstrated. We have presented the design, growth, and characterization of MWIR HPTs based on type-II InAs/AlSb/GaSb superlattices. The devices with 60 nm base thickness exhibited 50% cut-off wavelengths of ~3.95 and ~4.05 mm at 77 and 150 K, respectively. A saturated optical gain of 668 and 639 at 77 and 150K, respectively, was measured. At 150 K, the collector dark current density is 1×10^{-3} A/cm^2. Also at 150 K, the device exhibited a specific detectivity of 4.4×10^{12} cm·Hz$^{1/2}$/W. This specific detectivity value is four times higher than a state-of-the-art T2SL-based photodiode with a similar cut-off wavelength. We have also studied the impact of scaling base thickness from 60 nm to 40 nm on the optical and electrical performance of T2SL base MWIR HPT devices. These devices show enhanced optical performance when the base thickness is decreased. The device with the thinnest base width (40 nm) exhibits the highest peak of responsivity as 9528 A W^{-1} under V_{CE} = 140 mV and 8845 A W^{-1} under V_{CE} = 230 mV at temperatures of 150 and 77 K, respectively. The specific detectivity values stay constant over a broad range of wavelengths and applied biases for all the measures HPT devices. The saturated optical gain for the device with 40 nm base thickness shows an enhancement by shrinking the size of the base. As a result of vertical scaling of the base, exceptional current gain was achieved, whereas high current gain limits electrical performance by creating an increase in collector dark current density for the thinnest base layer.

In conclusion, this work has shown that it is possible to create high performance gain-based MWIR photodetectors based on type-II InAs/AlSb/GaSb superlattices. Thanks to the extreme bandstructure tunability of this material system, T2SL-based HPTs can help facilitate development of high-speed free-space optical communication systems in the MWIR region as well as better MWIR imagers (compared to those based on conventional photodiodes).

REFERENCES

[1] A. Pavelchek, R. G. Trissel, J. Plante, and S. Umbrasas, "Long-wave infrared (10-μm) free-space optical communication system," 2004, pp. 247-252.

[2] J. M. Kahn, "Secure free-space optical communication between moving platforms," in *Lasers and Electro-Optics Society, 2002. LEOS 2002. The 15th Annual Meeting of the IEEE*, 2002, pp. 455-456 vol.2.

[3] J. R. Minch, D. R. Gervais, and D. J. Townsend, "Adaptive Transceivers for Mobile Free-Space Optical Communications," in *Military Communications Conference, 2006. MILCOM 2006. IEEE*, 2006, pp. 1-5.

[4] A. Hood, A. Evans, and M. Razeghi, "Type-II superlattices and quantum cascade lasers for MWIR and LWIR free-space communications," 2008, pp. 690005-690005-9.

[5] F. Capasso, W. T. Tsang, C. G. Bethea, A. L. Hutchinson, and B. F. Levine, "New graded band-gap picosecond phototransistor," *Applied Physics Letters,* vol. 42, pp. 93-95, 1983.

[6] H. Kroemer, "Heterostructure bipolar transistors: What should we build?," *Journal of Vacuum Science & Technology B,* vol. 1, pp. 126-130, 1983.

[7] M. Rezaei, M. S. Park, C. L. Tan, and H. Mohseni, "Sensitivity limit of nanoscale phototransistors," *arXiv preprint arXiv:1704.05987,* 2017.

[8] J. C. Campbell and K. Ogawa, "Heterojunction phototransistors for long-wavelength optical receivers," *Journal of Applied Physics,* vol. 53, pp. 1203-1208, 1982.

[9] S. Mallick, K. Banerjee, S. Ghosh, E. Plis, J. B. Rodriguez, S. Krishna, *et al.*, "Ultralow noise midwave infrared InAs–GaSb strain layer superlattice avalanche photodiode," *Applied Physics Letters,* vol. 91, p. 241111, 2007.

[10] O. G. Memis, A. Katsnelson, S.-C. Kong, H. Mohseni, M. Yan, S. Zhang, *et al.*, "Sub-Poissonian shot noise of a high internal gain injection photon detector," *Optics Express,* vol. 16, pp. 12701-12706, 2008/08/18 2008.

[11] V. Fathipour, S. J. Jang, I. H. Nia, and H. Mohseni, "Impact of three-dimensional geometry on the performance of isolated electron-injection infrared detectors," *Applied Physics Letters,* vol. 106, p. 021116, 2015.

[12] C. Joe, A. Dentai, C. Burrus, and J. Ferguson, "InP/InGaAs heterojunction phototransistors," *IEEE Journal of Quantum Electronics,* vol. 17, pp. 264-269, 1981.

[13] H. Kroemer, "Heterostructure bipolar transistors and integrated circuits," *Proceedings of the IEEE,* vol. 70, pp. 13-25, 1982.

[14] H. Livingston, "A survey of heterojunction bipolar transistor (HBT) device reliability," *IEEE Transactions on Components and Packaging Technologies,* vol. 27, pp. 225-228, 2004.

[15] P. Asbeck, M.-C. F. Chang, J. Higgins, N. Sheng, and G. Sullivan, "GaAlAs/GaAs heterojunction bipolar transistors-Issues and prospects for application," *IEEE Transactions on Electron Devices,* vol. 36, pp. 2032-2042, 1989.

[16] M. Feng, N. Holonyak, and W. Hafez, "Light-emitting transistor: Light emission from InGaP/GaAs heterojunction bipolar transistors," *Applied Physics Letters,* vol. 84, pp. 151-153, 2004.

[17] C. S. Ozkan and A. Salmi, "Heterojunction bipolar transistor (HBT) fabrication using a selectively deposited silicon germanium (SiGe)," ed: Google Patents, 2003.

[18] Y.-W. Chen, W.-C. Hsu, R.-T. Hsu, Y.-H. Wu, Y.-J. Chen, and Y.-S. Lin, "Investigation of InGaP/GaAs heterojunction bipolar transistor with doping graded base," *Journal of Vacuum Science & Technology B,* vol. 21, pp. 2555-2557, 2003.

[19] P. Zingway, C. S. Liang, L. S. Lai, Y. T. Tseng, Y. M. Hsu, P. S. Chen, *et al.*, "A high-performance SiGe-Si multiple-quantum-well heterojunction phototransistor," *IEEE Electron Device Letters,* vol. 24, pp. 643-645, 2003.

[20] Sai, x, G. A. Halasz, R. Tsu, and L. Esaki, "A new semiconductor superlattice," *Applied Physics Letters,* vol. 30, pp. 651-653, 1977.

[21] A. M. Hoang, A. Dehzangi, S. Adhikary, and M. Razeghi, "High performance bias-selectable three-color Short-wave/Mid-wave/Long-wave Infrared Photodetectors based on Type-II InAs/GaSb/AlSb superlattices," *Scientific Reports,* vol. 6, p. 24144, 04/07/online 2016.

[22] A. Haddadi, A. Dehzangi, R. Chevallier, S. Adhikary, and M. Razeghi, "Bias–selectable nBn dual–band long–/very long–wavelength infrared photodetectors based on InAs/InAs1−xSbx/AlAs1−xSbx type–II superlattices," *Scientific Reports,* vol. 7, p. 3379, 2017/06/13 2017.

[23] A. Haddadi, A. Dehzangi, S. Adhikary, R. Chevallier, and M. Razeghi, "Background-limited long wavelength infrared InAs/InAs1-xSbx type-II superlattice-based photodetectors operating at 110K," *APL Materials,* vol. 5, p. 5, 2017.

[24] M. Razeghi, A. Haddadi, A. Dehzangi, R. Chevallier, and T. Yang, "Recent advances in InAs/InAs1-xSbx/AlAs1-xSbx gap-engineered type-II superlattice-based photodetectors," in *Proc. SPIE 10177, Infrared Technology and Applications XLIII, 1017705* 2017, pp. 1017705-1017705-11.

[25] M. Razeghi, A. Haddadi, A. M. Hoang, R. Chevallier, S. Adhikary, and A. Dehzangi, "InAs/InAs1-xSbx type-II superlattices for high performance long wavelength infrared detection," in *Proc. SPIE 9819, Infrared Technology and Applications XLII, 981909,* 2016, pp. 981909-981909-8.

[26] A. Haddadi, S. Adhikary, A. Dehzangi, and M. Razeghi, "Mid-wavelength infrared heterojunction phototransistors based on type-II InAs/AlSb/GaSb superlattices," *Applied Physics Letters,* vol. 109, p. 021107, 2016.

[27] B.-M. Nguyen, D. Hoffman, P.-Y. Delaunay, E. K.-W. Huang, M. Razeghi, and J. Pellegrino, "Band edge tunability of M-structure for heterojunction design in Sb based type II superlattice photodiodes," *Applied Physics Letters,* vol. 93, p. 163502, 2008.

[28] M. Razeghi, A. Haddadi, X. V. Suo, S. Adhikary, P. Dianat, R. Chevallier, *et al.*, "High-performance short-wavelength infrared photodetectors based on type-II InAs/InAs1-xSbx/AlAs1-xSbx superlattices," in *Proc. SPIE 9819, Infrared Technology and Applications XLII*, 2016, pp. 98190A-98190A-7.

[29] N. Binh-Minh, C. Guanxi, H. Minh-Anh, and M. Razeghi, "Growth and Characterization of Long-Wavelength Infrared Type-II Superlattice Photodiodes on a 3-in GaSb Wafer," *Quantum Electronics, IEEE Journal of,* vol. 47, pp. 686-690, 2011.

[30] G. G. Zegrya and A. D. Andreev, "Mechanism of suppression of Auger recombination processes in type-II heterostructures," *Applied Physics Letters,* vol. 67, pp. 2681-2683, 1995.

[31] A. Haddadi, R. Chevallier, A. Dehzangi, and M. Razeghi, "Extended short-wavelength infrared nBn photodetectors based on type-II InAs/AlSb/GaSb superlattices with an AlAsSb/GaSb superlattice barrier," *Applied Physics Letters,* vol. 110, p. 101104, 2017.

[32] M. Razeghi, "Focal Plane Arrays in Type-II Superlattices," US Patent 6864552, 2005.

[33] A. Dehzangi, A. Haddadi, R. Chevallier, Y. Zhang, and M. Razeghi, "nBn extended short–wavelength infrared focal plane array," *Optics Letters,* vol. under press, 2018.

[34] R. Chevallier, A. Dehzangi, A. Haddadii, and M. Razeghi, "Type-II superlattice-based extended short-wavelength infrared focal plane array with an AlAsSb/GaSb superlattice etch-stop layer to allow near-visible light detection," *Optics Letters,* vol. 42, pp. 4299-4302, 2017/11/01 2017.

[35] Y. Wei, A. Gin, M. Razeghi, and G. J. Brown, "Type II InAs/GaSb superlattice photovoltaic detectors with cutoff wavelength approaching 32 μm," *Applied Physics Letters,* vol. 81, pp. 3675-3677, 2002.

[36] S. A. Pour, E. K. Huang, G. Chen, A. Haddadi, B.-M. Nguyen, and M. Razeghi, "High operating temperature midwave infrared photodiodes and focal plane arrays based on type-II InAs/GaSb superlattices," *Applied Physics Letters,* vol. 98, p. 143501, 2011.

[37] A. Dehzangi, A. Haddadi, S. Adhikary, and M. Razeghi, "Impact of scaling base thickness on the performance of heterojunction phototransistors," *Nanotechnology*, vol. 28, p. 10LT01, 2017.

[38] A. Hood, D. Hoffman, B.-M. Nguyen, P.-Y. Delaunay, E. Michel, and M. Razeghi, "High differential resistance type-II InAs/GaSb superlattice photodiodes for the long-wavelength infrared," *Applied Physics Letters,* vol. 89, p. 093506, 2006.

[39] N. Chand, P. A. Houston, and P. N. Robson, "Gain of a heterojunction bipolar phototransistor," *IEEE Transactions on Electron Devices,* vol. 32, pp. 622-627, 1985.

[40] A. M. Hoang, G. Chen, A. Haddadi, S. Abdollahi Pour, and M. Razeghi, "Demonstration of shortwavelength infrared photodiodes based on type-II InAs/GaSb/AlSb superlattices," *Applied Physics Letters,* vol. 100, p. 211101, 2012.

[41] B. Yu, L. Wang, Y. Yuan, P. M. Asbeck, and Y. Taur, "Scaling of Nanowire Transistors," *IEEE Transactions on Electron Devices,* vol. 55, pp. 2846-2858, 2008.

[42] A. Dehzangi, F. Larki, M. M. R. Wee, N. Wichmann, B. Y. Majlis, and S. Bollaert, "Analog/RF Study of Self-aligned In0. 53Ga0. 47As MOSFET with Scaled Gate Length," *Journal of Electronic Materials,* vol. 46, pp. 782-789, 2017.

[43] M. F. Mohd Razip Wee, A. Dehzangi, S. Bollaert, N. Wichmann, and B. Y. Majlis, "Gate Length Variation Effect on Performance of Gate-First Self-Aligned In0.53Ga0.47As MOSFET," *PLOS ONE,* vol. 8, p. e82731, 2013.

[44] R. Jae-Sung, D. Greenberg, A. Stricker, and G. Freeman, "Scaling of SiGe Heterojunction Bipolar Transistors," *Proceedings of the IEEE,* vol. 93, pp. 1522-1538, 2005.

[45] A. F. J. Levi, B. Jalali, R. N. Nottenburg, and A. Y. Cho, "Vertical scaling in heterojunction bipolar transistors with nonequilibrium base transport," *Applied Physics Letters,* vol. 60, pp. 460-462, 1992.

[46] W. Hafez, W. Snodgrass, and M. Feng, "12.5 nm base pseudomorphic heterojunction bipolar transistors achieving fT=710GHz and fMAX=340GHz," *Applied Physics Letters,* vol. 87, p. 252109, 2005.

[47] S. M. Sze and K. K. Ng, *Physics of Semiconductor Devices*: Wiley, 2006.

[48] A. Elfving, G. V. Hansson, and W. X. Ni, "SiGe (Ge-dot) heterojunction phototransistors for efficient light detection at 1.3–1.55 μm," *Physica E: Low-dimensional Systems and Nanostructures,* vol. 16, pp. 528-532, 3// 2003.

[49] M. N. Abedin, T. F. Refaat, O. V. Sulima, and U. N. Singh, "AlGaAsSb-InGaAsSb HPTs with high optical gain and wide dynamic range," *IEEE Transactions on Electron Devices,* vol. 51, pp. 2013-2018, 2004.